

## TTVs analysis in Southern Stars: the case of WASP-28

R. Petrucci<sup>1,3,4</sup>, E. Jofré<sup>2,3,4</sup>, M. Melita<sup>1,3</sup>, M. Gómez<sup>2,3</sup>, and P. J. D. Mauas<sup>1,3</sup>

Received \_\_\_\_\_; accepted \_\_\_\_\_

---

<sup>1</sup>Instituto de Astronomía y Física del Espacio (IAFE), Buenos Aires, Argentina.

<sup>2</sup>Observatorio Astronómico de Córdoba, Córdoba, Argentina.

<sup>3</sup>CONICET, Consejo Nacional de Investigaciones Científicas y Técnicas, Argentina.

<sup>4</sup>Visiting Astronomer, Complejo Astronómico El Leoncito operated under agreement between the Consejo Nacional de Investigaciones Científicas y Técnicas de la República Argentina and the National Universities of La Plata, Córdoba and San Juan.

## ABSTRACT

We present 4 new transit observations of the exoplanet WASP-28b observed between August 2011 and October 2013. Employing another 11 transits available in the literature we compute new ephemeris and redetermine the physical parameters of the star and the exoplanet. Considering 3 yrs of observations, we find no periodic TTVs or long-term variations of the inclination of the orbit,  $i$ , or the depth of the transit,  $k$ , that could be attributable to the presence of another planetary mass-body in the system. We also study the relations between  $i$  and  $k$  with different factors that characterize the light-curves. The fits suggest a possible weak correlation between  $k$  with the red noise factor,  $\beta$ , and the photometric noise rate, PNR, and a weak anticorrelation between  $i$  and PNR, although more points are needed to confirm these trends. Finally, the kinematic study suggests that WASP-28 is a thin disk star.

*Subject headings:* stars: individual: WASP-28 — techniques: photometric — planetary systems

## 1. Introduction

To date, more than 1400<sup>1</sup> exoplanets have been discovered. Most of them were mainly detected by the radial velocity (Mayor & Queloz 1995; Marcy & Butler 1996) and the transit (Charbonneau et al. 2000; Henry et al. 2000) techniques. The former method is based on the detection of periodic Doppler shifts in the stellar spectral lines due to the movement of the star around the star-planet barycenter. The second one is based upon the detection of periodic variations of the stellar flux produced by the passage of a planet in front of the stellar disk. In the last years, a new technique became very popular to search for planets: the transit timing variations or TTVs (Holman & Murray 2005; Díaz et al. 2008). In a system composed only by a star and a transiting planet, one should expect that the interval between successive minima be constant. However, if there is a third body in the system, periodic variations of this interval are anticipated. Therefore, it should be possible to detect other planetary-mass bodies around stars with an already known transiting planet. The less massive the perturber, the smaller the amplitudes of the timing variations, and the higher precision minimum central times (with errors of around seconds) are required. Many factors have to be taken into account to reach realistic conclusions about TTVs: sampling of the observations (Kipping 2010), quality of the light curves, presence of red noise (Carter & Winn 2009; Barros et al. 2013; Lendl et al. 2013), variable atmospheric conditions during the night (for ground-base observations), etc. In addition, as it has been shown in several studies (e.g. Southworth et al. 2012; Nascimbeni et al. 2013), for TTV analysis it is of crucial relevance to perform the same fitting procedure and error treatment in the transits studied.

On the other hand, there is evidence suggesting that the probability of finding gas giant planets around main-sequence stars is an increasing function of the stellar metallicity,

---

<sup>1</sup>Extracted from <http://exoplanet.eu/catalog/>

reaching only 3% for stars with subsolar metallicity (Fischer & Valenti 2005; Santos et al. 2004, 2005). With a  $[\text{Fe}/\text{H}] = -0.29$  dex, the F8 star WASP-28 (Anderson et al. 2014) seems to fall in the metal-poor long tail of the metallicity distribution of the planet-host stars. The planet around this star, WASP-28b, discovered by the SuperWASP program (?), is a Hot Jupiter-like planet ( $M_{\text{P}} = 0.907 M_{\text{Jup}}$ ,  $R_{\text{P}} = 1.213 R_{\text{Jup}}$  and  $a = 0.044$  AU) describing a prograde and aligned orbit. The age of the system ( $5_{-2}^{+3}$  Gyr) suggests the possibility that the current orbit of the planet could be reached by planet-disc migration or via tidal interaction although, if the last possibility is assumed, the fact that the planet had not fallen into the star remains unexplained. In this sense, it becomes relevant the study of TTVs to understand the dynamic history of the system (e.g. Ford 2014). In a recent work, Steffen et al. (2012) conclude that, in contrast to the presence of transit timing variations in systems with long-period Jupiters, hot-Neptunes and hot-Earths, the absence of TTVs in Hot-Jupiter systems might indicate different planet formation and dynamical evolution theories. The authors suggest that the main mechanism responsible for the formation of Hot-Jupiters could be the planet-planet scattering.

In this work we carried on a complete and homogeneous study of TTVs and looked for variations in the photometric parameters of WASP-28b. We considered the influence of many factors related to the quality of the studied light-curves to explain the high dispersions found in the long-term behaviour of the parameters. Finally, we investigated whether the low metallicity of WASP-28 can be due to its galactic population membership, through the calculation of its galactic spatial velocities.

This article is organized as follows: in Section §2 we present our observations and data reduction. In Section §3 we describe the procedure used to fit the light-curves and to derive the photometric and physical parameters. In Section §4 we discuss the long-term variations of the parameters and calculate the relation between them and different factors

that characterize the light-curves. In Section §5 we carry out a TTVs study of the system and calculate new ephemeris. In Section §6 we describe the kinematic properties of WASP-28 and discuss possible scenarios for the formation of its Hot Jupiter in a metal-poor environment. Finally, in Section §7 we present the conclusions.

## 2. Observations and data reduction

The 4 transits of WASP-28b were observed between August 2011 and October 2013. The observations were carried out with the Telescope Horacio Ghilmetti (THG) located at Cerro Bureck in the Complejo Astronómico El Leoncito (San Juan, Argentina). This telescope is a remotely-operated MEADE-RCX 400 with a 40-cm primary mirror and Johnson UBVRI filters. The transit corresponding to 2012, July 26 was observed using an Apogee Alta U8300 camera with  $3326 \times 2504$   $5\mu$  pixels, with a scale of  $0.32''/\text{pix}$  and a  $19' \times 14'$  field of view. The remaining ones were observed employing an Apogee Alta U16M camera with  $4096 \times 4096$   $9\mu$  pixels, resulting in a scale of  $0.57''/\text{pix}$  and a  $49' \times 49'$  field of view. For the transit of 2013 October 26, the images were strongly defocused to minimize the dispersion of the resulting transit. After testing different bin sizes and filters, we decided to use a bin of  $2 \times 2$  to achieve a better temporal resolution. We adopted integration times ranging from 10 to 120 sec depending on seeing, airmass conditions and the selected filter. In Table 1 we present a log of the observations.

Before every observation the computer clock was automatically synchronized with the GPS time signal, to be certain that the times of all the images were expressed in Heliocentric Julian Date based on Coordinated Universal Time ( $HJD_{\text{UTC}}$ ). For each night, we took 10 bias and 8 dark frames. We averaged all the biases and median combined the

bias-corrected darks. We employed the standard IRAF<sup>2</sup> tasks to perform bias and dark correction. We did not perform the flat-fielding correction to the images, since we found that it introduced unwanted errors.

All the instrumental magnitudes were obtained with the FOTOMCC pipeline (Petrucci et al. 2013), which employs aperture photometry choosing the optimal annulus through the growth-curves technique (Howell 1989). Once the instrumental magnitudes were obtained, we carried out the differential photometry.

As one of the purposes of this work is to study TTVs, we decided to include all other transits publicly available. Besides ours, we employed 11 light-curves published in the Exoplanet Transit Database (ETD<sup>3</sup>). We considered only those where the transits were clearly visible.

The smooth trends present in the light-curves are mainly originated by differences between the spectral types of the comparison and the exoplanet host-star, differential extinction and, occasionally, by stellar activity. To remove these trends, for each light-curve we selected the before-ingress and after-egress data-points and fitted a second order Legendre polynomial. Only in a few cases a first order polynomial was applied. Then, we removed the fit from all the data (including transit points) and normalized the out-of-transit (OOT) data to unit.

---

<sup>2</sup>IRAF is distributed by the National Optical Astronomy Observatories, which are operated by the Association of Universities for Research in Astronomy, Inc., under cooperative agreement with the National Science Foundation.

<sup>3</sup><http://var2.astro.cz/ETD>

### 3. Determination of the parameters

#### 3.1. Photometric parameters

We derived fundamental stellar parameters and metallicity ( $T_{\text{eff}}$ ,  $\log g$ ,  $\xi$ , [Fe/H]) for WASP-28 using HARPS archival spectra<sup>4</sup>. A total of 33 individual spectra were co-added to produce a single spectrum with an average signal-to-noise of around 100:1, suitable for spectroscopic analysis.

These four quantities were derived in LTE using the FUNDPAR<sup>5</sup> fortran code (Saffe 2011). This program determines fundamental parameters from a list of Fe lines equivalent widths, using the 2010 version of the MOOG code (Snedden 1973), and calculates Kurucz ATLAS plane-parallel model atmospheres. Equivalent widths for 27 Fe I and 12 Fe II weak and isolated lines were measured automatically using the ARES code (Sousa et al. 2007). The resulting values obtained from the analysis are:  $T_{\text{eff}} = 6084 \pm 45$  K,  $\log g = 4.51 \pm 0.03$  cm s<sup>-1</sup>,  $\xi = 2 \pm 0.12$  km s<sup>-1</sup>, [Fe/H] =  $-0.2 \pm 0.07$  dex. These results agree with the values of the fundamental parameters published by Anderson et al. (2014). However, our uncertainties in  $T_{\text{eff}}$  and  $\log g$  are much smaller than those calculated by Anderson et al. (2014), probably due to the different method used to compute these parameters.

We calculated theoretical limb-darkening coefficients with the program JKTLTD<sup>6</sup> by bilinear interpolation of the effective temperature and surface gravity using the tabulations of Claret (2004), which were built employing Kurucz ATLAS9 atmospheric models. As

---

<sup>4</sup>Based on observations collected at the La Silla Paranal Observatory, ESO (Chile) with the HARPS spectrograph at the 3.6-m telescope, programme ID 085.C-0393(A).

<sup>5</sup>Available at <http://icate-conicet.gob.ar/saffe/fundpar/>

<sup>6</sup><http://www.astro.keele.ac.uk/jkt/codes/jktld.html>

these tabulations do not provide theoretical limb-darkening coefficients for the Johnson-R filter, for those transits observed in this band we adopted the values tabulated for the Cousin-R filter. For the light-curves obtained with no filter, we took the average of the values corresponding to the Johnson-V and Cousin-R bands.

We used the JKTEBOP code<sup>7</sup> to fit all the light-curves. This code assumes that the star and the planet have biaxial ellipsoid projections and computes the light-curve considering concentric circles over each component. For each transit, initially we assumed as adjusted parameters the inclination ( $i$ ), the sum of the fractional radii ( $\Sigma = r_{\star} + r_{\text{P}}$ ) and the ratio of the fractional radii ( $k = r_{\text{P}}/r_{\star}$ ). Here,  $r_{\star} = R_{\star}/a$  and  $r_{\text{P}} = R_{\text{P}}/a$  represent the ratios of the absolute radii of the star and the exoplanet, respectively, to the semimajor axis ( $a$ ). We also took as free parameters the mid-transit time ( $T_0$ ) and the scale factor ( $l_0$ ). We adopted as initial parameters for the iteration those determined by Anderson et al. (2014). We calculated  $k$  and  $\Sigma$  employing the values of  $R_{\star}$ ,  $R_{\text{P}}$  and  $a$  computed in the same paper. As in Southworth et al. (2012) every light-curve was fitted with four different limb darkening laws: linear, quadratic, logarithmic and square-root. For each law, we tried three different possibilities: 1) both coefficients fixed, 2) the linear coefficient fitted and the nonlinear fixed and, 3) both coefficients fitted. Finally, we adopted as the best model for a given light-curve the one with minimum  $\chi^2$  and realistic values for the adjusted parameters. To get  $\chi_r^2 = 1$ , we multiplied the photometric errors by the square-root of the reduced chi-squared of the fit. Finally, since the Levenberg-Marquardt optimization algorithm we employed to get the best-fitting model only computes formal errors for the adjusted parameters, we ran two other tasks implemented in JKTEBOP: Monte Carlo simulations (for which we took 10000 iterations) and the residual permutation (RP) algorithm which takes the presence of red noise into account. We assumed the median value of the empirical

---

<sup>7</sup><http://www.astro.keele.ac.uk/jkt/codes/jktebop.html>

data as the final value of each parameter (except for  $T_0$ , see Section §5), and its error was conservatively adopted as the largest value obtained for both tasks. In Fig. 1 we show the 15 transits and the best fit to the data and in Table 2 we list the photometric parameters determined for each light-curve.

To obtain realistic results, we considered only the values of  $i$ ,  $k$  and  $\Sigma$  obtained from the high quality and complete light-curves of our sample. A way to evaluate the light-curve quality is to calculate the photometric noise rate (PNR). In Fulton et al. (2011) this parameter is defined as:

$$PNR = \frac{rms}{\sqrt{\Gamma}}, \quad (1)$$

where  $rms$  is the standard deviation of the light-curve residuals and  $\Gamma$  is the median number of exposures (including not only the exposure time but also the readout time) per minute. In our case, we considered as the best quality light-curves those with PNR lower than 5 mmag. Then, taking into account only the values of the photometric parameters of these complete and high quality transits (5 points), we computed the values and errors of  $i$ ,  $k$  and  $\Sigma$  as the weighted average and the standard deviation of the sample, respectively. The final estimations of these parameters are:

$$\begin{aligned} i &= 87.92 \pm 0.45 \\ k &= 0.127 \pm 0.013 \\ \Sigma &= 0.131 \pm 0.006 \end{aligned}$$

Although JKTEBOP gives less certain but still useful results when light-curves are incomplete<sup>8</sup>, to determine how well the Levenberg-Marquardt optimization algorithm explores the parameter space for partial transits, we tested the influence of the initial parameters in the final results. Therefore, for the 8 incomplete transits of our sample

---

<sup>8</sup>John Southworth, private communication.

we computed the photometric parameters adopting as initial values those published by Anderson et al. (2014)  $\pm 3$  times the error<sup>9</sup>, alternatively. In the first case we named the final parameters  $i_+$ ,  $k_+$  and  $\Sigma_+$  and  $i_-$ ,  $k_-$  and  $\Sigma_-$  in the latter case. In Table 3, we show the differences between the parameters listed in Table 2 and those obtained as we explained before. Except for the transits of the epochs 160 and 367, all the differences remain within the errors. The two outliers correspond to the poorest-quality light-curves according to the factor PNR (see column 8 of Table 2). **These results indicate that, because the transit equation is non linear, the Levenberg-Marquardt algorithm can be trapped in a local minimum (which may not be the global minimum) and hence, might not correctly explore the parameter space.**

### 3.2. Physical parameters

To determine the physical parameters we employed the JKTABSDIM code<sup>10</sup>. This code uses standard formulae (Southworth 2009) to calculate the absolute dimensions of a system with two components, from the results of radial velocity and light-curve analysis. As input, it requires the photometric quantities ( $i$ ,  $r_*$ ,  $r_P$ ) obtained in the previous section, the orbital period ( $P$ ) determined from the ephemeris, the stellar velocity amplitude ( $K_*$ ), for which we adopted the value given by Anderson et al. (2014), the eccentricity, for which we assumed a circular orbit ( $e = 0$ ), the velocity amplitude of the planet ( $K_P$ ), and the

---

<sup>9</sup>For  $i$ ,  $k$  and  $\Sigma$  we considered as errors those calculated through the 5 best light-curves. For  $l_0$  and the limb-darkening coefficients we assumed 0.001 and 0.01, respectively.

<sup>10</sup><http://www.astro.keele.ac.uk/~jkt/codes/jktabsdim.html>

corresponding errors<sup>11</sup>.

The value chosen for  $K_P$  was the one which minimizes the figure of merit:

$$fom = \left[ \frac{r_{\star}^{(\text{obs})} - (R_{\star}^{(\text{calc})}/a)}{\sigma(r_{\star}^{(\text{obs})})} \right]^2 + \left[ \frac{T_{\text{eff}}^{(\text{obs})} - T_{\text{eff}}^{(\text{calc})}}{\sigma(T_{\text{eff}}^{(\text{obs})})} \right]^2, \quad (2)$$

where the predicted radius ( $R_{\star}^{(\text{calc})}$ ) and effective temperature ( $T_{\text{eff}}^{(\text{calc})}$ ) of the star were determined by linearly interpolating the calculated stellar mass<sup>12</sup> and  $[\text{Fe}/\text{H}]$ <sup>13</sup> within tabulated theoretical models. To avoid any dependence of the resulting parameters with the employed stellar-model we performed this analysis for 3 different tabulated models:  $Y^2$  (Demarque et al. 2004), Padova (Girardi et al. 2010) and Teramo (Pietrinferni et al. 2004). For each one, we considered series of isochrones bracketing the lifetime of the star in the main-sequence. In this way, it was possible to estimate the age of the system. We adopted as final value for  $K_P$  the average of the amplitudes given by each model, and for the velocity error we used the standard deviation. Therefore, by applying this procedure, we obtained  $M_{\star}$ ,  $R_{\star}$ ,  $\log g_{\star}$ ,  $M_P$ ,  $R_P$ ,  $a$  and age.

For completeness, we calculated the exoplanet surface gravity with (Southworth et al. 2007):

$$g_P = \frac{2\pi}{P} \frac{\sqrt{(1-e^2)}K_{\star}}{r_P^2 \sin(i)}, \quad (3)$$

and the modified equilibrium temperature (Southworth 2010) as:

---

<sup>11</sup>For the photometric parameters we considered the error as the larger between  $\sigma_+$  and  $\sigma_-$ .

<sup>12</sup>The stellar mass was computed from Eq. (5) of Southworth (2009).

<sup>13</sup>We adopted the value  $[\text{Fe}/\text{H}] = -0.2$  dex, determined in the previous section.

$$T'_{\text{eq}} = T_{\text{eff}} \sqrt{\frac{R_{\star}}{2a}}, \quad (4)$$

assuming that the planetary albedo is zero. In Table 4 we present our results. The final values for the physical properties and their errors were calculated considering the photometric parameters determined in Section §3.1, which were computed from the best 5 light-curves. All these parameters are in good agreement, within errors, with the values reported in the discovery paper by Anderson et al. (2014).

#### 4. Long-term variations of the parameters

Since the presence of a perturber (moon or another planet) could produce periodic variations of the depth and/or inclination, in Fig. 2 we show the long-term behaviour of these parameters. It can be seen that in both cases there are points which apart more than  $\pm 1\sigma$  from the mean value. We computed the Lomb-Scargle periodogram (Horne & Baliunas 1986) to see if there are any periodicities which could be attributed to the presence of a perturber, but we did not find any significant peak. To discern the origin of these dispersions we studied the correlation between the photometric parameters and different factors related to the quality of the light-curves.

##### 4.1. Incomplete transits

We investigated if the lack of transit points influences the adjusted parameters. In Fig. 3 we indicate with empty symbols the incomplete transits and in filled symbols the complete ones. It can be seen in Table 5 that the distributions overlap and the median values are similar within an error of  $\pm\sigma$ . This means that, even in the absence of some points in the light-curves, we should expect reliable values for the adjusted parameters  $i$  and

k. However, this result could be contaminated by other factors (such as white and/or red noises) and most importantly, as we showed in Section §3.1, for partial transits the Levenberg-Marquardt algorithm might not correctly explore the parameter space. In this sense, our conclusion agrees with the one found by recent works (Gibson et al. 2009; Barros et al. 2011, 2013) which show that incomplete transits could affect the values and errors of the system parameters obtained from these light-curves. Therefore in the following subsections we exclude partial transits from our analysis.

#### 4.2. Filter

Seager & Mallén-Ornelas (2003) show in Fig 11 how observations of transits with low impact parameters, taken in filters with  $\lambda \geq 1 \mu$  can increase the depth of the transit up to 25%. Since WASP-28 has  $b = 0.21$  and half of the transits studied in this work were observed with no filter and half in the R-band, we analysed if there is a correlation between the measured depth and the employed filter. In the lower panel of Fig. 3 we show with red circles the transits observed in the R-filter and in blue triangles those observed with no filter (and one in the B-band). To determine if both datasets represent the same population we calculated the median and  $\pm\sigma$  of the samples (see Table 6) only using complete transits. We could not make a Kolmogorov-Smirnov test because the number of data in both samples is lower than 10. By performing a visual inspection and considering the data in Table 6, we concluded that there is no evident trend and both distributions overlap. This can be interpreted as that the band in which the transits were observed has no influence in the final  $k$  values. In the upper panel of Fig. 3, it can be noticed that the same conclusion is reached regarding the inclination,  $i$ .

### 4.3. Red Noise

This is the noise produced by systematic errors due to changes in atmospheric conditions, airmass, telescope tracking, relative flat field errors, or a combination of all these factors. It can also be caused by the intrinsic variability of the targets. The presence of red noise in the data implies that adjacent data points in a light-curve are correlated (Pont et al. 2006). Although it is not completely well understood, the existence of this kind of noise leads to an underestimation of the errors in the adjusted parameters, resulting in an inaccurate determination of them. Red noise can be quantified with the factor  $\beta = \sigma_r/\sigma_N$ , defined by Winn et al. (2008). Here,  $\sigma_r$  is obtained by averaging the residuals into  $M$  bins of  $N$  points and calculating the standard deviation of the binned residuals, and  $\sigma_N$  is the expected standard deviation, calculated by:

$$\sigma_N = \frac{\sigma_1}{\sqrt{N}} \sqrt{\frac{M}{M-1}}, \quad (5)$$

where  $\sigma_1$  is the standard deviation of the unbinned residuals. In our case, to estimate the parameter  $\beta$ , we considered that the duration of the ingress/egress of the WASP-28b transits is around 20 minutes, and we averaged the residuals in bins of between 10 and 30 minutes. Finally, we used the median value as the red noise factor corresponding to that light-curve. In column 7 of Table 2, we show the values obtained. Since in the absence of red noise  $\beta = 1$ , we see that in almost all transits white noise predominates.

In the lower panel of Fig. 4 we show the variation of depth with  $\beta$  for complete transits. The red continuous line represents the best linear fit to the data obtained through weighted least-squares. As it can be seen, there is a weak positive correlation indicating that noisier

observations result in larger depths. Considering all the points,  $r = 0.381$ , but if we exclude the transit with  $\beta = 2.2$ ,  $r$  increases to 0.577. This figure seems to suggest that observations with large red noise would lead to an overestimation of the planetary radius.

In the upper panel of Fig. 4, we plot the variation of  $i$  with the red noise. Contrary to what occurs with  $k$ , the correlation between these parameters is almost zero ( $r = 0.0059$ ), indicating that the values of the inclination are not influenced by the presence of red noise.

#### 4.4. Photon Noise Rate

Fig. 5 shows the variation of  $i$  and  $k$  with PNR for complete transits. In the lower panel we present  $k$  vs PNR. It can be seen that there is a correlation ( $r = 0.335$ ), similar to the one found for  $\beta$ , which indicates that low-quality data can result in overestimations of the planetary radius for a given value of the stellar radius. On the other hand, the values of  $i$  are slightly anticorrelated ( $r = -0.269$ ) with PNR, showing that noisy transits could lead to underestimations of the values of the inclination.

### 5. Transit ephemeris and timing

As the minimum central times are uncorrelated with the rest of the parameters, we fitted each one of the 15 individual transit light curves considering  $T_0$  as the only adjusted parameter. For the fixed parameters we adopted the final values obtained in Section §3.1 .

We used the Eastman et al. (2010) on-line converter to transform the times of all the observations to  $BJD_{\text{TDB}}$  (Barycentric Julian Date based on Barycentric Dynamical Time). We assumed that the  $T_0$  have a Gaussian distribution, and therefore we adopted for the mid-transit times the mean values and the symmetric errors ( $\pm\sigma$ ) given by the best fit

to the light-curves. As we explained in Section §3, the errors considered are the largest between the estimated by Monte Carlo and by the RP algorithms.

In Table 7 we present the mid transit times computed for all the light-curves. If we include all the 15 points into the analysis, we find a  $\chi_r^2 = 3.27$  which seems to suggest the possibility of variations in the data. However, as it can be noted in Fig. 6, there are 5 outliers that strongly deviate from the rest of data. All of these correspond to incomplete transits (magenta triangles). Gibson et al. (2009) show that in a large percentage of cases, the mid-times of partial transits are unrealistic. They attribute this to the fact that a lack of points in the OOT data affects the symmetry of the light-curve and hence the central transit times, due to an incorrect normalisation. On the other hand, the points of the epochs 159, 358 and 367 correspond to transits with high level of red noise (all of them with  $\beta \geq 1$ ), while the ones corresponding to the epochs 160, 358 and 367 belong to low quality light-curves. Fulton et al. (2011) show that the inclusion of big outliers can lead to false conclusions about the existence of TTVs. Taking all this into account we decided to exclude all partial transits from our analysis to sure that they are not biasing the results. To calculate the best period ( $P$ ) and the minimum reference time ( $T_{\text{minref}}$ ), we fitted a linear model to the 7 remaining data through weighted least-squares. The new ephemeris obtained are:

$$T_0(E) = T_{\text{minref}} + E * P \tag{6}$$

where  $P = 3.408840 \pm 0.000003$  days and  $T_{\text{minref}} = 2455290.40551 \pm 0.00102$  BJD<sub>TDB</sub>. Here  $E$  represents the epoch. The uncertainties were obtained from the covariance matrix of the fit and were re-scaled multiplying them by  $\sqrt{\chi_r^2}$ . In this case,  $\chi_r^2 = 0.7$ , implying that the measurements agree with a linear ephemeris and there is no evident periodic variations in the O-C diagram. As it is shown in Fig. 6, the point corresponding to the epoch 382 is outside the area between the  $\pm 1\sigma$  dashed lines. We cannot explain the cause of this

anomalous value.

Since the version of the JKTEBOP code employed in this work (version 28) does not permit to normalise the out-of-transit data-points and to fit the light-curves simultaneously, both processes were carried out separately. However, recent works (Gibson et al. 2009; Barros et al. 2013) have noticed that the measured transit-times would correlate with the normalisation function, suggesting that the normalisation parameters should be taken into account during the fitting procedure.

For completeness, we investigated the mass of a possible perturber, considering different orbital configurations. To do that, we assumed an external perturbing body whose semimajor axis is much greater than that of the transiting planet and used the Eq. (2) from Holman & Murray (2005):

$$M_2 = \frac{16}{45\pi} M_\star \frac{\Delta t}{P_1} \left( \frac{P_2}{P_1} \right)^2 (1 - e_2)^3 \quad (7)$$

where,  $P_1$  and  $P_2$  are the orbital periods of WASP-28b and the perturber, respectively,  $M_\star$  is the stellar mass,  $e_2$  is the eccentricity of the perturber and  $\Delta t$  represents the variations in the interval between successive transits. For  $P_1$  and  $M_\star$ , we assumed the values obtained in previous sections and for  $\Delta t$  we adopted 3.6 minutes, which is the standard deviation of the 7 points considered to do the TTV analysis. For the perturber, we tested the following values for the eccentricity: 0, 0.001, 0.01, 0.05, 0.1 and 0.25 and semimajor axes from 0.08 to 0.35 AU with step 0.01. In Fig. 7 we showed the results obtained. For clarity, we cut the graph in  $M_2 = 8 M_{\text{Jup}}$  and  $a_2 = 0.3$  AU. If we consider a very eccentric orbit for the perturber ( $e = 0.25$ ) and a semimajor axis almost the double of the semimajor axis of the transiting planet ( $a = 0.08$  AU), our TTVs precision would permit to set the maximum mass of an undetected perturber in more than half of the Saturn mass ( $M_2 = 0.21 M_{\text{Jup}}$ ). Under the supposition that the perturbing body has a circular orbit ( $e = 0$ ) and ( $a = 0.08$  AU), its mass would be half of the Jupiter mass.

We also investigated the masses of possible external perturbers located in the positions of first-order mean-motion resonances with WASP-28b. We employed the Eq. (33) from Agol et al. (2005):

$$\Delta t = \frac{P_1}{4.5j} \frac{M_2}{M_2 + M_1} \quad (8)$$

where  $j$  is the number of orbits between conjunctions. We calculated the values of  $\Delta t$  for the first-order resonances 2:1, 3:2, 4:3 and 5:4, ranging the mass of the perturber from  $1 M_{\oplus}$  to  $10 M_{\text{Jup}}$  with step 0.001. Considering our TTVs dispersion, the results permit to rule out the presence of a perturber with a mass greater than 1.9, 2.8, 3.8 and  $4.7 M_{\oplus}$  at the 2:1, 3:2, 4:3 and 5:4 resonances with WASP-28b. It is important to notice that this is just a first approximation and a more rigorous analysis of the resonances, employing equations of motion, should be done in order to obtain more precise results.

## 6. Kinematic properties of WASP-28

In order to establish the Galaxy population membership of the metal-poor star WASP-28, we computed its kinematic properties. The galactic-velocity components ( $U, V, W$ ) and their errors were calculated following the methodology described in Sections III and IV of Johnson & Soderblom (1987). We assumed the same directions for  $V$  and  $W$ , but for the  $U$ -component we supposed the opposite direction to the one adopted in that paper. To do the calculation, we used as initial quantities:  $RA(2000) = 353.616$ ,  $DEC(2000) = -01.580$ ,  $pmRA = 22.5 \pm 1.3 \text{ mas yr}^{-1}$ ,  $pmDEC = 7.8 \pm 1.3 \text{ mas yr}^{-1}$ ,  $RV = 24.33 \pm 0.02 \text{ km s}^{-1}$  and  $\pi = 2.439 \pm 0.014 \text{ mas}$ . The values of  $pmRA$  and  $pmDEC$  were taken from Zacharias et al. (2003), the radial velocity was calculated from the same HARPS spectra employed to determine the photometric parameters, whereas the rest of the parameters were taken from Anderson et al. (2014). The parallax ( $\pi$ ) was calculated from the value of distance published in that paper. The final space-velocity

components were derived relative to the Local Standard of Rest assuming a solar motion of  $(U, V, W)_{\odot} = (-10.00, +5.25, +7.17)$  (Dehnen & Binney 1998). The resulting values for WASP-28 are:  $U_{\text{LSR}} = 34.56 \text{ km s}^{-1}$ ,  $V_{\text{LSR}} = 12.84 \text{ km s}^{-1}$ ,  $W_{\text{LSR}} = -19.12 \text{ km s}^{-1}$ . Based on these velocities we investigated the Galactic population membership of WASP-28 considering the probabilities that the star belongs to the thick or thin disk or the halo ( $p_{\text{thin}}, p_{\text{thick}}, p_{\text{halo}}$ ). To compute these probabilities, we employed the Eq. (1) and (2) of Reddy et al. (2006) obtaining the following values:  $p_{\text{thin}} = 0.985$ ,  $p_{\text{thick}} = 0.014$ ,  $p_{\text{halo}} = 3.27 \times 10^{-5}$ , which suggest that WASP-28 is a thin disk star. Therefore, this star might have been formed in some of the metal-poor clouds of the local neighborhood.

In the last years several works (Ghezzi et al. 2010; Johnson et al. 2010; Johnson & Li 2012; Maldonado et al. 2013) have discussed the scenario for the formation of planets around metal-poor stars (or planets in the low metallicity tail of the planet-metallicity correlation), like WASP-28. In the core accretion model (Pollack et al. 1996) a threshold density of solid material in the protoplanetary disk is necessary for a rapid growth of planetesimals. Once a massive enough core is formed, it can accrete an atmosphere forming a gas-giant planet which can migrate close to the star, before the gas dissipates. This model is strongly dependent on the metallicity of the cloud (Matsuo et al. 2007). This means that the larger the metallicity the faster the formation of the giant planet, giving it enough time to migrate to distances less than 0.1 AU. But, if the metallicity of the disk is low, the growth of planetesimals is slower. Therefore, when the giant planet is completely formed, much of the gas near the star is already dissipated, and the recently formed planet cannot migrate too close to the star. Therefore, protoplanetary disks with low metallicity would have a scarce probability of forming Hot Jupiters. However, Natta et al. (2000) showed that high-mass stars would have massive protoplanetary disks. Recently, Alibert et al. (2011) and Mordasini et al. (2012) showed that giant planet formation can take place in protoplanetary disks with low metallicity and high mass. In this scenario,

the required limit of metal content to form a Jupiter-like planet would be lower for disks around high-mass stars than for disks surrounding less massive stars. Johnson et al. (2010) also showed that giant-planet frequency is an increasing function of not only the metallicity but also the stellar mass, and hence of the mass of the disk. In this scenario, the stellar mass would compensate the protoplanetary-disk low metallicity, allowing the formation of Jupiter-like planets (Kennedy & Kenyon 2009; Ghezzi et al. 2010; Johnson et al. 2010, and references therein). As it was noted by Ida & Lin (2004) and Laughlin et al. (2004) if the disk mass increases, then the surface density of the protoplanetary disk increases, favoring the formation of gas giant planets in the core accretion model.

Another possibility is the gravitational-instability model of Boss (2006). Boss (1997, 2002) proposed this mechanism to explain the formation of giant planets before the dissipation of gas in the disk. In this scenario, if the protoplanetary disk is massive enough, it could break up in dense fragments. Typically, in several hundreds of years these fragments would contract to form giant proto-planets. In this situation, the planets form quickly, before the gas depletion. Contrary to the core-accretion theory, this model is almost independent on  $[\text{Fe}/\text{H}]$ . Furthermore, Cai et al. (2006) and Meru & Bate (2010) pointed out that the efficiency of the formation of giant planets through disk instability decreases as the metallicity increases.

Considering that WASP-28 is an intermediate-mass star, we can assume that its protoplanetary disk was of intermediate mass. In this scenario, both models could explain the origin of WASP-28b. On one hand, if the planet was formed through the core accretion model, the low-metallicity disk could have been compensated by the required density of solid material provided by the mass in the disk. If the planet was formed by Boss' model, the abundant mass of the protoplanetary disk would have been enough to allow the fragmentation and consecutive collapse of the resulting proto-planets.

## 7. Conclusions

In this work we presented observations of 4 new transits of the system WASP-28, observed between August 2011 and October 2013. Additionally, we also studied 11 transits reported by other observers, which were downloaded from the Exoplanet Transit Database.

We performed an homogeneous study of the 15 transits, and obtained new ephemeris and redetermined the parameters of the system. To look for evidence of another planetary-mass body present in the system, we analysed the long-term variations of  $i$  and  $R_P/R_\star$ , finding large scattering in some points but without evidence of a periodic pattern. We found a weak anticorrelation between the noise of the observations (measured by PNR) and the  $i$  measured in the transit, indicating that the inclination measured in noisy transits could be underestimated. For  $R_P/R_\star$ , we found a possible correlation with red noise and PNR, which would suggest that noisy light-curves, would lead to overestimate the planetary radius for a given value of  $R_\star$ . However it is important to caution that these relations are based on a small number of points ( $N = 7$ ) and a statistically significant sample is needed to confirm these trends.

We performed the first TTV analysis of this system. We found that the  $O - C$  are well fitted by a linear ephemeris, with the exception of several outliers, which correspond to incomplete transits and very noisy observations. Therefore, we found no evidence of the presence of another body in the system.

On the other hand, the dynamical analysis showed that for our TTVs precision the maximum mass that a perturber could have is  $M_2 = 0.21 M_{Jup}$ , considering an eccentric orbit. However, if the orbit of the perturber is circular the maximum mass should be of  $M_2 = 0.51 M_{Jup}$ . In the case of 2:1, 3:2, 4:3 and 5:4 first-order resonances we found that our data permit to exclude a external perturber with mass greater than 1.9, 2.8, 3.8 and 4.7  $M_\oplus$  respectively.

Finally, we performed the first study of the kinematic properties of WASP-28. We measured the components of the galactic velocity ( $U_{LSR}$ ,  $V_{LSR}$ ,  $W_{LSR}$ ) and found that there is a probability of 0.94 that the star belongs to the thin disk.

### Acknowledgments

We thank Martín Schwartz for his valuable work in the maintenance and operation of the THG, Pablo Perna and the Casleo staff for technical support, and CONICET for funding this research. R.P. also thanks John Southworth for useful comments and Andrea Buccino for her help with the references. R.P. and E.J. are also grateful to A. Sabella for the motivation. We also thank the anonymous referee for his/her useful comments and suggestions, mainly those corresponding to the Sections 3.1 and 4.1, which really helped to improve the quality of this paper. This research has made use of the SIMBAD database, operated at CDS, Strasbourg, France and NASA's Astrophysics Data System.

## REFERENCES

- Agol E., Steffen J., Sari R., Clarkson W., 2005, MNRAS, 359, 567
- Alibert Y., Mordasini C., Benz W., 2011, A&A, 526, A63
- Anderson, D. R., Collier Cameron, A., Lendl, M., Maxted, P. F. L., Queloz, D., Smalley, B., Smith, A. M., Triaud, A. H. M. J., et al. 2014, preprint (arXiv:e-prints)
- Barros S. C. C., Boué G., Gibson N. P., Pollacco D. L., Santerne A., Keenan F. P., Skillen I., Street R. A., 2013, MNRAS, 430, 3032
- Barros S. C. C., Pollacco D. L., Gibson N. P., Howarth I. D., Keenan F. P., Simpson E. K., Skillen I., Steele I. A., 2011, MNRAS, 416, 2593
- Boss A. P., 1997, Science, 276, 1836
- Boss A. P., 2002, ApJ, 567, L149
- Boss A. P., 2006, ApJ, 637, L137
- Cai, K., Durisen, R. H., Michael, S., et al. 2006, ApJ, 636, 149
- Carter J. A., Winn J. N., 2009, ApJ, 704, 51
- Charbonneau, D., Brown, T. M., Latham, D. W., Mayor, M., 2000, ApJ, 529, L45
- Claret, A. 2004, A&A, 428, 1001
- Dehnen W., Binney J. J., 1998, MNRAS, 298, 387
- Demarque, P., Woo, J. H., Kim, Y. C., & Yi, S. K., 2004, ApJS, 155, 667
- Díaz R. F., Rojo P., Melita M., Hoyer S., Minniti D., Mauas P. J. D., Ruíz M. T., 2008, ApJ, 682, L49

- Eastman, J., Siverd, R., & Gaudi, B. S., 2010, *PASP*, 122, 935
- Fischer D. A., Valenti J., 2005, *ApJ*, 622, 1102
- Ford E. B., 2014, ArXiv e-prints
- Fulton B. J., Shporer A., Winn J. N., Holman M. J., Pál A., Gazak J. Z., 2011, *AJ*, 142, 84
- Ghezzi L., Cunha K., Schuler S. C., Smith V. V., 2010, *ApJ*, 725, 721
- Ghezzi L., Cunha K., Smith V. V., de Araújo F. X., Schuler S. C., de la Reza R., 2010, *ApJ*, 720, 1290
- Gibson N. P., Pollacco D., Simpson E. K., Barros S., Joshi Y. C., Todd I., Keenan F. P., Skillen I., Benn C., Christian D., Hrudková M., Steele I. A., 2009, *ApJ*, 700, 1078
- Girardi, L., Bressan, A., Bertelli, G., Chiosi, C., 2000, *A&AS*, 141, 371
- Henry G. W., Marcy G. W., Butler R. P., Vogt S. S., 2000, *ApJ*, 529, L41
- Holman, M. J., & Murray 2005, *Science*, 307, 1288
- Horne, J. H. & Baliunas, S. L. 1986, *ApJ*, 302, 757
- Howell, S. B. 1989, *PASP*, 101, 616
- Ida S., Lin D. N. C., 2004, *ApJ*, 616, 567
- Johnson D. R. H., Soderblom D. R., 1987, *AJ*, 93, 864
- Johnson J. A., Aller K. M., Howard A. W., Crepp J. R., 2010, *PASP*, 122, 905
- Johnson J. L., Li H., 2012, *ApJ*, 751, 81
- Kennedy G. M., Kenyon S. J., 2009, *ApJ*, 695, 1210

- Kipping D. M., 2010, MNRAS, 408, 1758
- Laughlin G., Bodenheimer P., Adams F. C., 2004, ApJ, 612, L73
- Lendl M., Gillon M., Queloz D., Alonso R., Fumel A., Jehin E., Naef D., 2013, A&A, 552, A2
- Maldonado J., Villaver E., Eiroa C., 2013, A&A, 554, A84
- Marcy, G. W., & Butler, R. P., 1996, ApJ, 464, L147
- Matsuo T., Shibai H., Ootsubo T., Tamura M., 2007, ApJ, 662, 1282
- Mayor, M., & Queloz, D., 1995, Nature, 378, 355
- Meru F., Bate M. R., 2010, MNRAS, 406, 2279
- Mordasini C., Alibert Y., Benz W., Klahr H., Henning T., 2012, A&A, 541, A97
- Nascimbeni, V., Cunial, A., Murabito, S. et al., 2013, A&A, 549, 30
- Natta A., Grinin V., Mannings V., 2000, Protostars and Planets IV, p. 559
- Petrucci R., Jofré E., Schwartz M., Cúneo V., Martínez C., Gómez M., Buccino A. P., Mauas P. J. D., 2013, ApJ, 779, L23
- Pietrinferni, A., Cassisi, S., Salaris, M., & Castelli, F., 2004, ApJ, 612, 168
- Pollacco, D. L., Skillen, I., Collier Cameron, A., Christian, D. J., Hellier, C., Irwin, J., Lister, T. A., Street, R. A., et al. 2006, PASP, 118, 1407
- Pollack J. B., Hubickyj O., Bodenheimer P., Lissauer J. J., Podolak M., Greenzweig Y., 1996, Icarus, 124, 62
- Pont, F., Zucker S., & Queloz, D., 2006, MNRAS, 373, 231

- Reddy B. E., Lambert D. L., Allende Prieto C., 2006, MNRAS, 367, 1329
- Saffe, C. 2011, RMxAA, 47, 3
- Santos N. C., Israelian G., Mayor M., 2004, A&A, 415, 1153
- Santos N. C., Israelian G., Mayor M., Bento J. P., Almeida P. C., Sousa S. G., Ecuivillon A., 2005, A&A, 437, 1127
- Seager, S., & Mallén-Ornelas, G., 2003, ApJ, 585, 1038
- Snedden, C, A. 1973, PhD thesis, Univ. of Texas
- Sousa S. G., Santos N. C., Israelian G., Mayor M., Monteiro M. J. P. F. G., 2007, A&A, 469, 783
- Southworth J., 2009, MNRAS, 394, 272
- Southworth J., 2010, MNRAS, 408, 1689
- Southworth J., Bruni I., Mancini L., Gregorio J., 2012, MNRAS, 420, 2580
- Southworth J., Wheatley P. J., Sams G., 2007, MNRAS, 379, L11
- Steffen J. H., Ragozzine D., Fabrycky D. C., Carter J. A., Ford E. B., Holman M. J., Rowe J. F., Welsh W. F., Borucki W. J., Boss A. P., Ciardi D. R., Quinn S. N., 2012, Proceedings of the National Academy of Science, 109, 7982
- Southworth, J., Wheatley, P. J., & Sams, G., 2007, MNRAS, 379, 11
- Winn J. N., Holman M. J., Torres G., McCullough P., Johns-Krull C., Latham D. W., Shporer A., Mazeh T., Garcia-Melendo E., Foote C., Esquerdo G., Everett M., 2008, ApJ, 683, 1076

Zacharias N., Urban S. E., Zacharias M. I., Wycoff G. L., Hall D. M., Germain M. E.,  
Holdenried E. R., Winter L., 2003, VizieR Online Data Catalog, 1289, 0

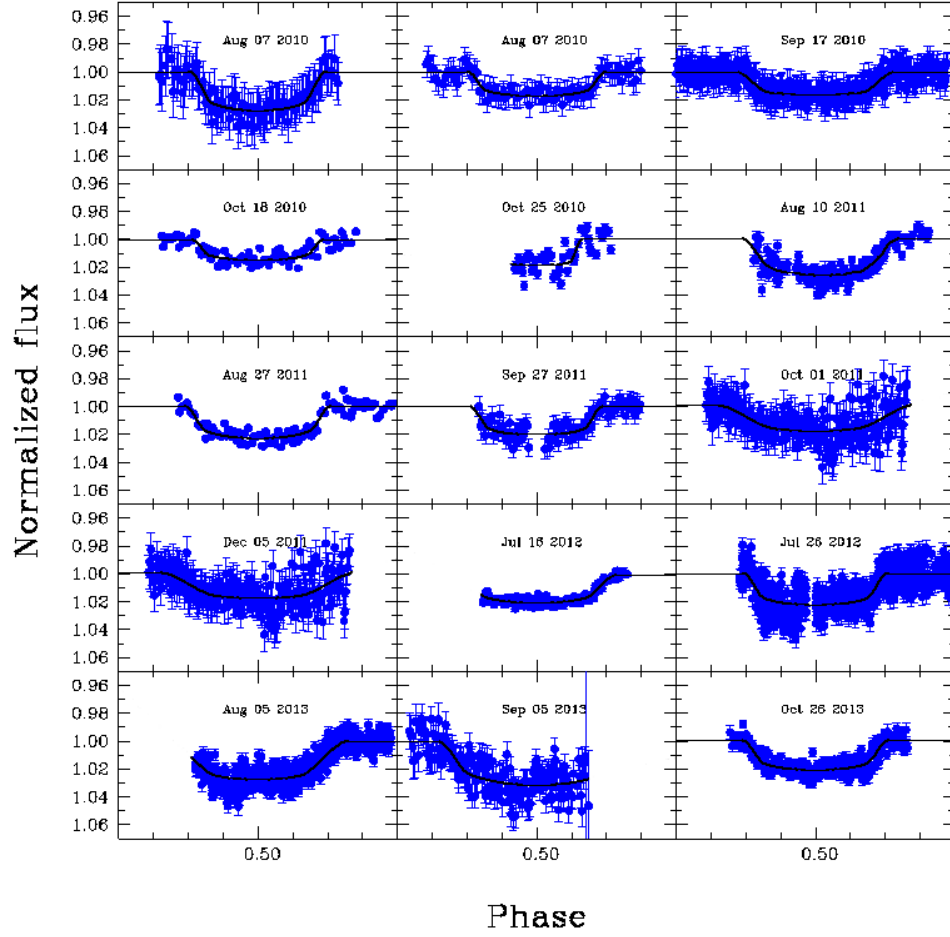


Fig. 1.— Transits analysed in this work. The photometric data and their error bars are marked in blue. Black solid lines represent the best fit to the data. We also indicate the date when the transits were observed.

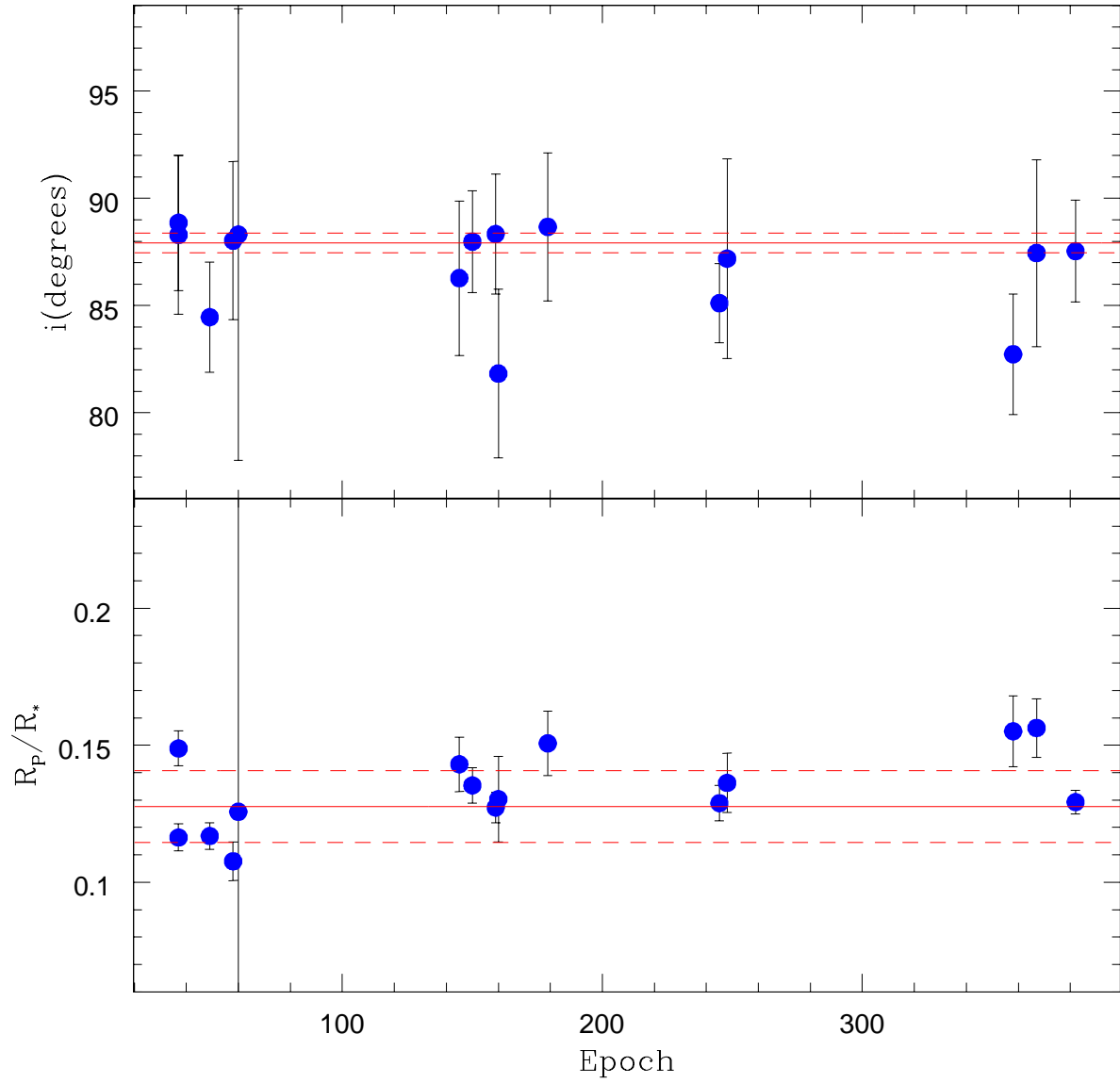


Fig. 2.— Long-term variation of  $i$  (upper panel) and  $k$  (lower panel). Continuous lines represent the weighted averages calculated in Section §3.1 and dashed lines indicate  $\pm 1\sigma$ . Error bars are also shown.

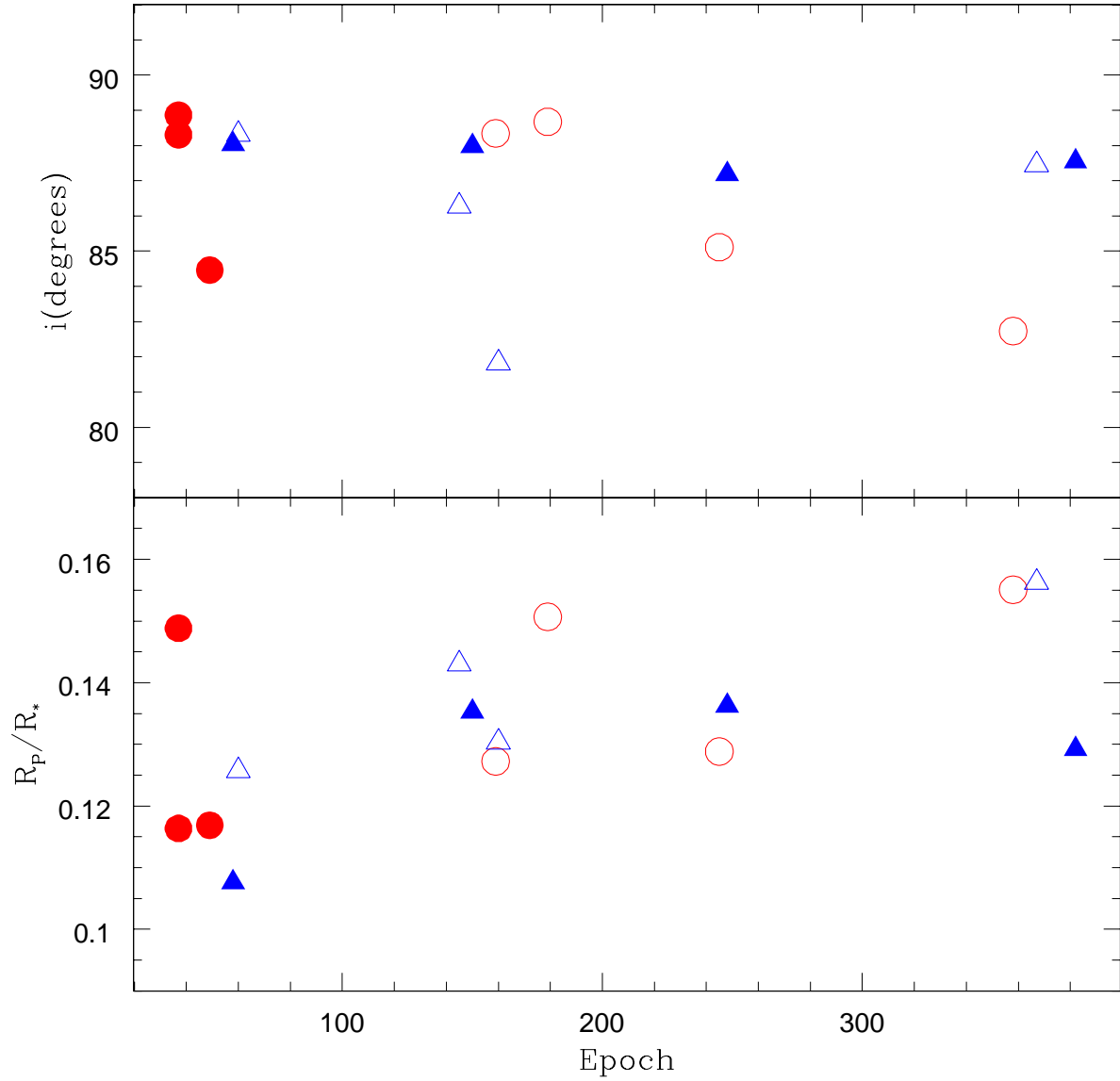


Fig. 3.— Long-term variation of  $i$  (upper panel) and  $k$  (lower panel). The filled and empty symbols indicate the complete and incomplete transits, respectively. Red circles correspond to the transits taken in the red filters and blue triangles to those observed in the blue filters (B or no filter).

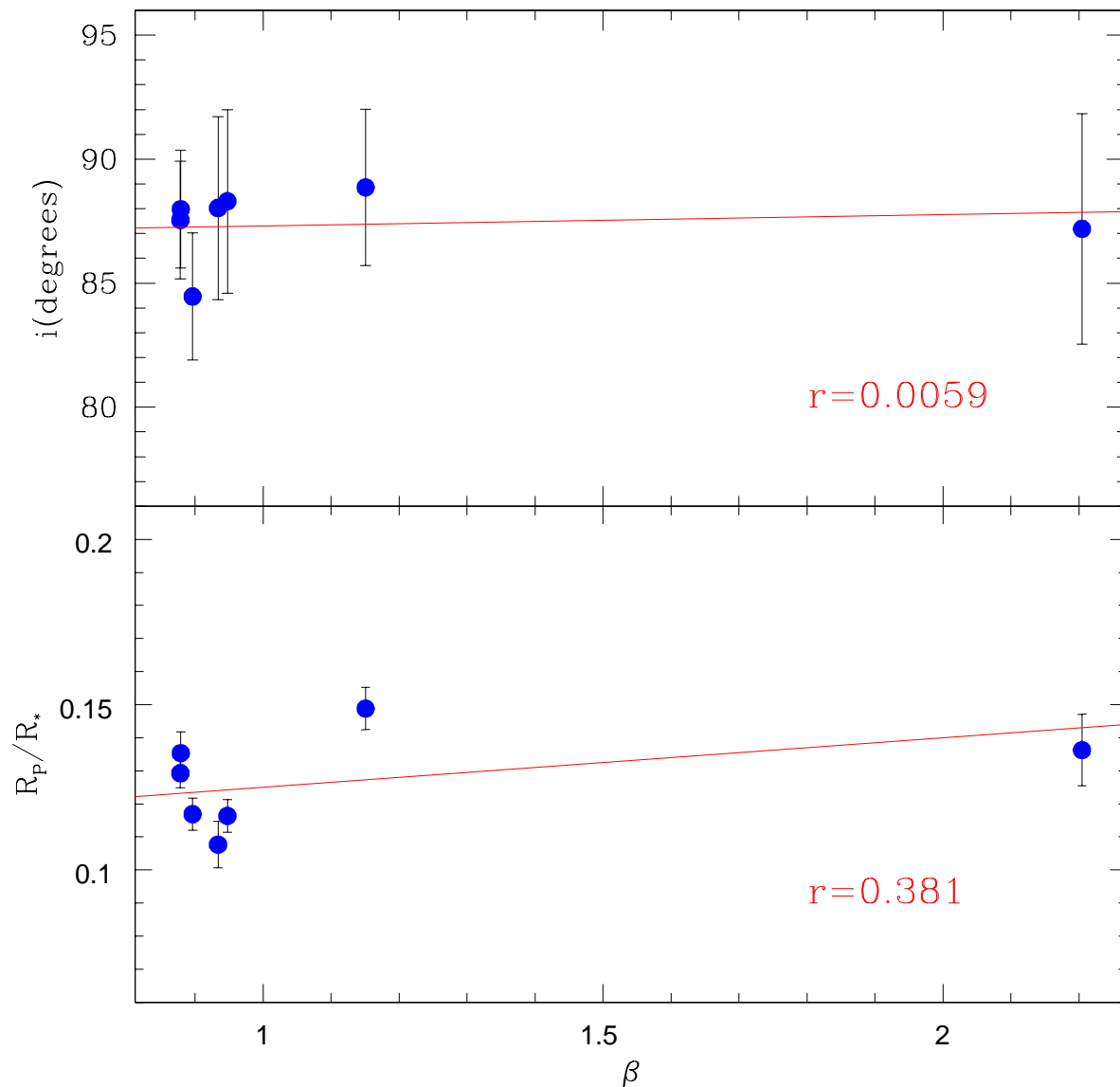


Fig. 4.— Variation of  $i$  and  $k$  with the red noise factor,  $\beta$ . The red continuous lines are the best linear fit to the data obtained through weighted least-squares. The correlation coefficients  $r$  are also shown. In the lower panel the  $r = 0.577$  is obtained excluding the point with the largest  $\beta$ . If it is included, the correlation coefficient is  $r = 0.381$ . Error bars are also shown.

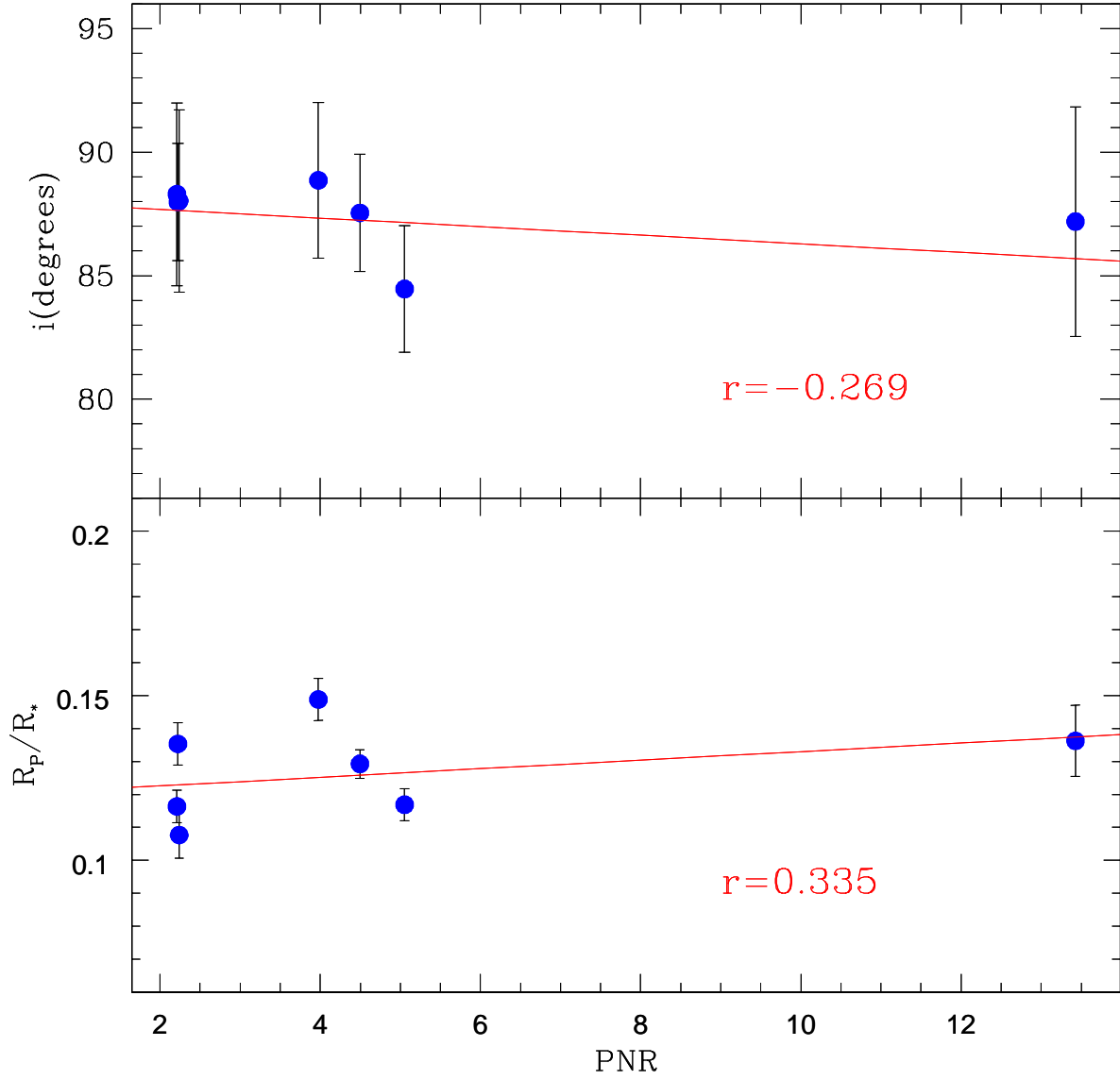


Fig. 5.— Variation of  $i$  and  $k$  with PNR. The red continuous lines are the best linear fit to the data obtained through weighted least-squares. Error bars are also shown.

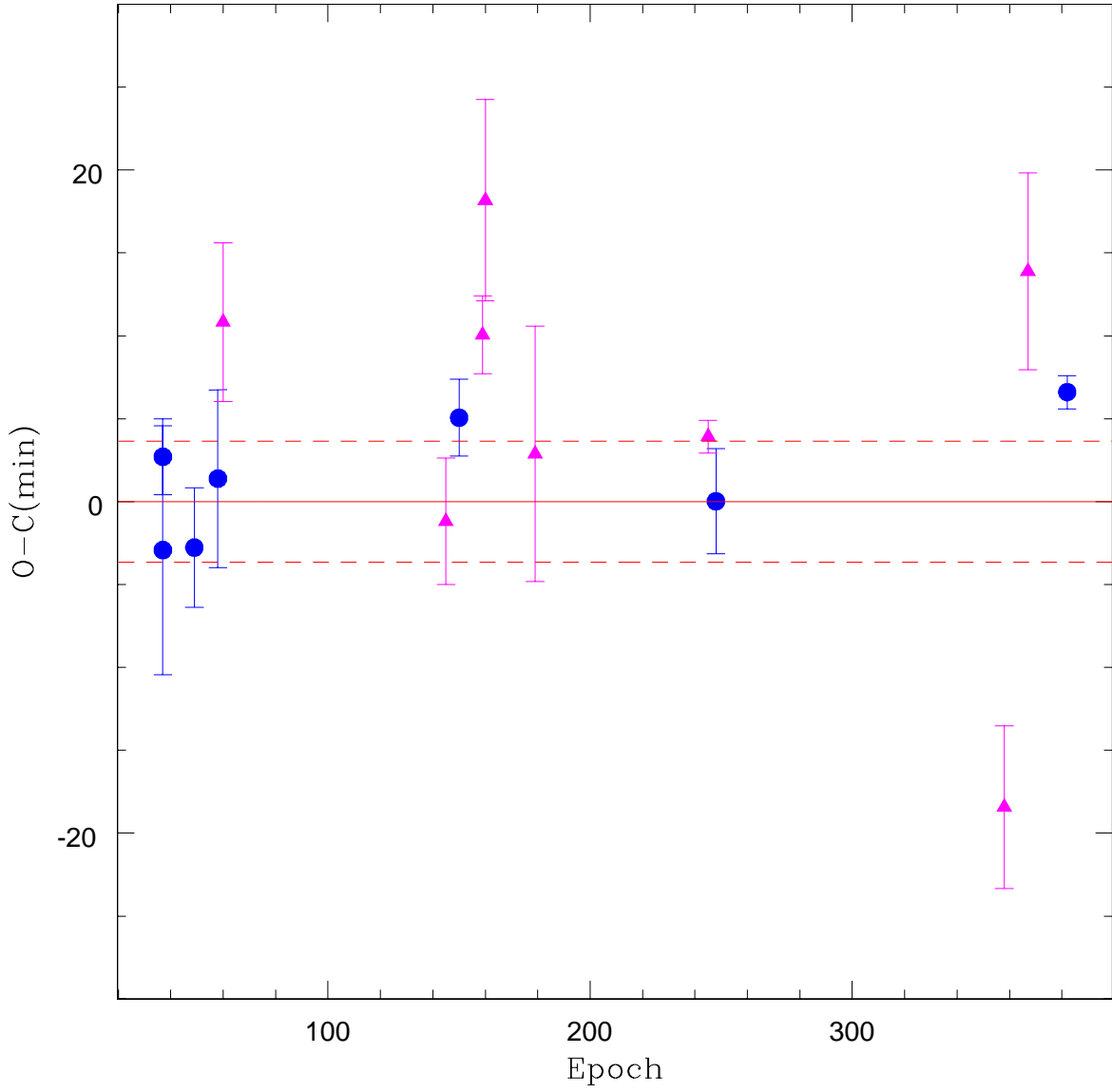


Fig. 6.— O-C diagram for transit timing of WASP-28b. Magenta triangles mark the points excluded from our calculation of the new ephemeris. Dashed lines indicate  $\pm 1\sigma$  considering only the blue circles.

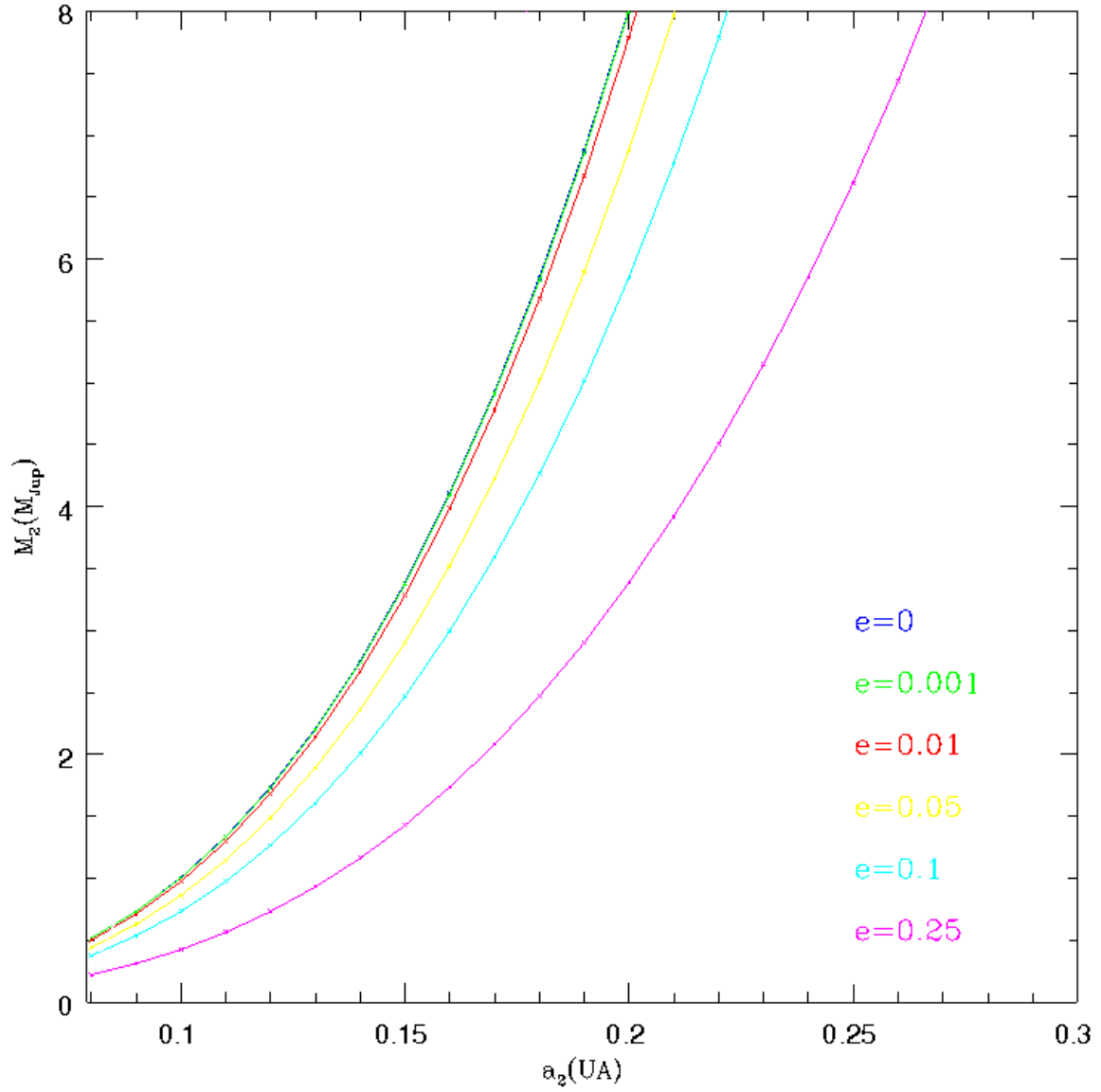


Fig. 7.— Semimajor axis vs mass of a possible perturbing body. Each color indicates a different eccentricity.

Table 1. Log of our observations.  $N_{obs}$  is the number of data-points and  $\sigma$  is the standard deviation of the out-of-transit data-points.

Date	Camera	Filter	Bin-size	Expsoure-Time (s)	$N_{obs}$	$\sigma$ (mag)
Aug 27 2011	U16M	no filter	1x1	120	105	0.0042
Jul 26 2012	U8300	no filter	4x4	10	711	0.0078
Aug 5 2013	U16M	R	2x2	30	407	0.0049
Oct 26 2013	U16M	no filter	2x2	50	231	0.004

Table 2. Characteristics of the Light Curves and Photometric Parameters Obtained

Date	Epoch	$i$	$k$	$\Sigma$	Filter	$\beta$	PNR (mmag)	Complete?	Reference
Aug 07 2010*	37	$88.86^{+1.1}_{-3.15}$	$0.1488^{+0.0059}_{-0.0064}$	$0.1244^{+0.0208}_{-0.0064}$	R	1.1508	3.977	Yes	1
Aug 07 2010*	37	$88.3^{+1.45}_{-3.7}$	$0.1164^{+0.0048}_{-0.0049}$	$0.1255^{+0.0220}_{-0.0066}$	R	0.9475	2.211	Yes	2
Sep 17 2010	49	$84.46^{+2.56}_{-2.51}$	$0.1169^{+0.0032}_{-0.0048}$	$0.1681^{+0.0304}_{-0.0273}$	R	0.8963	5.053	Yes	3
Oct 18 2010*	58	$88.03^{+1.9}_{-3.69}$	$0.1076^{+0.0070}_{-0.0051}$	$0.1215^{+0.0367}_{-0.0081}$	no filter	0.9337	2.239	Yes	4
Oct 25 2010	60	$88.31^{+1.65}_{-10.52}$	$0.1257^{+0.0140}_{-0.1248}$	$0.0901^{+0.0447}_{-0.0231}$	no filter	0.8813	3.949	No	4
Aug 10 2011	145	$86.28^{+3.6}_{-1.89}$	$0.1431^{+0.0100}_{-0.0062}$	$0.1439^{+0.0296}_{-0.0156}$	B	0.9776	4.362	No	5
Aug 27 2011*	150	$87.98^{+1.86}_{-2.37}$	$0.1353^{+0.0044}_{-0.0064}$	$0.1357^{+0.0205}_{-0.0069}$	no filter	0.8789	2.223	Yes	6
Sep 27 2011	159	$88.34^{+1.21}_{-2.8}$	$0.1272^{+0.0056}_{-0.0050}$	$0.1231^{+0.0227}_{-0.0079}$	R	1.2533	3.191	No	7
Oct 1 2011	160	$81.83^{+2.27}_{-3.93}$	$0.1303^{+0.0156}_{-0.0124}$	$0.2122^{+0.0697}_{-0.0348}$	no filter	1.0963	8.906	No	8
Dec 5 2011	179	$88.67^{+1.26}_{-3.46}$	$0.1507^{+0.0118}_{-0.0068}$	$0.1275^{+0.0224}_{-0.0075}$	R	1.4977	5.509	No	8
Jul 16 2012	245	$85.11^{+1.84}_{-1.24}$	$0.1288^{+0.0044}_{-0.0065}$	$0.1636^{+0.0157}_{-0.0165}$	R	0.7990	1.818	No	9
Jul 26 2012	248	$87.19^{+2.57}_{-4.65}$	$0.1363^{+0.0108}_{-0.0107}$	$0.1402^{+0.0366}_{-0.0148}$	no filter	2.2044	13.428	Yes	6
Aug 5 2013	358	$82.73^{+2.26}_{-2.81}$	$0.1551^{+0.0129}_{-0.0063}$	$0.2004^{+0.0513}_{-0.0300}$	R	1.7519	7.727	No	6
Sep 5 2013	367	$87.45^{+2.17}_{-4.36}$	$0.1563^{+0.0106}_{-0.0071}$	$0.1879^{+0.0533}_{-0.0273}$	no filter	1.3380	8.518	No	10
Oct 26 2013*	382	$87.54^{+2.37}_{-1.69}$	$0.1293^{+0.0044}_{-0.0035}$	$0.1369^{+0.0155}_{-0.0089}$	no filter	0.8783	4.495	Yes	6

\*Transits used to calculate the final values of  $i$ ,  $k$  and  $\Sigma$ . Columns 3-5: Values of the derived photometric parameters and their errors. Column 7: Median value for the red noise. Column 8: Photon noise rate. References: (1) Lorenz E. R. (TRESKA); (2) Naves R. (TRESKA); (3) Saral G. (TRESKA); (4) Curtis I. (TRESKA); (5) Makely N., Pree C. D. (TRESKA); (6) This work; (7) Gillier Ch. (TRESKA); (8) Shadic S. (TRESKA); (9) Sauer T. (TRESKA); (10) Pouzenc C. (TRESKA).

Table 3: Differences between  $i$ ,  $k$  and  $\Sigma$  and the values computed as it is explained in the text, for partial transits

Epoch	$\Delta i_+$	$\Delta k_+$	$\Delta \Sigma_+$
60	0.3	0.000384	0.0009
145	0.43	-0.001754	-0.0023
159	0.27	-0.001447	-0.0021
160	5.54	-0.018349	-0.0645
179	-0.24	0.00213	-0.0019
245	-0.16	0.000861	0.0029
358	0.02	-0.00029	0.0001
367	0.12	-0.000478	-0.0002
	$\Delta i_-$	$\Delta k_-$	$\Delta \Sigma_-$
60	-0.01	0.002184	-0.0009
145	0.4	-5.4E-05	-0.0048
159	-0.13	0.000753	-0.0012
160	-4.9	0.030651	0.0854
179	0.21	0.00413	-0.0039
245	-0.47	0.001861	0.0056
358	0	0.00021	-0.0005
367	-7.48	0.023822	0.0782

Table 4: Physical Properties of the Star and the Exoplanet

Parameter	Value
Stellar Mass $M_{\star}$ ( $M_{\odot}$ )	$1.011 \pm 0.028$
Stellar Radius $R_{\star}$ ( $R_{\odot}$ )	$1.123 \pm 0.052$
Stellar gravity $\log g_{\star}$ (cgs)	$4.342 \pm 0.040$
Planet Mass $M_{\text{P}}$ ( $M_{\text{Jup}}$ )	$0.899 \pm 0.035$
Planet Radius $R_{\text{P}}$ ( $R_{\text{Jup}}$ )	$1.354 \pm 0.166$
Planet equilibrium temperature $T_{\text{eq}}$ (K)	$1473 \pm 30$
Planet surface gravity $\log g_{\text{P}}$ (cgs)	$3.083 \pm 0.091$
Semimajor axis $a$ ( $UA$ )	$0.0445 \pm 0.0004$
Age (Gyr)	$4.2 \pm 1.0$

Table 5: Median value and standard deviation for  $i$  and  $k$  considering complete or incomplete transits

Transit	$i_{\text{median}}$	$\sigma_i$	$k_{\text{median}}$	$\sigma_k$
Complete	87.98	1.43	0.129	0.014
Incomplete	86.86	2.64	0.136	0.013

Table 6: Median value and standard deviation for  $i$  and  $k$  considering red or blue filters.

Filter	$i_{\text{median}}$	$\sigma_i$	$k_{\text{median}}$	$\sigma_k$
Red	88.3	2.39	0.116	0.018
Blue	87.76	0.39	0.132	0.013

Table 7: Mid-transit times

Epoch	$T_0$ ( $BJD_{\text{TDB}}$ )	$e_{T_0}$ ( $BJD_{\text{TDB}}$ )	Reference
37	2455416.529869	0.005214	1
37	2455416.533777	0.001582	2
49	2455457.435933	0.002501	3
58	2455488.118293	0.003719	4
60	2455494.942504	0.003327	4
145	2455784.684716	0.002644	5
150	2455801.733205	0.00161	6
159	2455832.416153	0.001629	7
160	2455835.830611	0.004218	8
179	2455900.587763	0.005352	8
245	2456125.571263	0.000681	9
248	2456135.795042	0.002203	6
358	2456510.753533	0.003411	6
367	2456541.455445	0.004124	10
382	2456592.582836	0.000698	6

References: (1) Lorenz E. R. (TRÉSCA); (2) Naves R. (TRÉSCA); (3) Saral G. (TRÉSCA); (4) Curtis I. (TRÉSCA); (5) Makely N., Pree C. D. (TRÉSCA); (6) This work; (7) Gillier Ch. (TRÉSCA); (8) Shadic S. (TRÉSCA); (9) Sauer T. (TRÉSCA); (10) Pouzenc C. (TRÉSCA).